PHYSICAL REVIEW B **101**, 134109 (2020)

Prediction of Fe_2P-type $TiTe_2$ under pressure

Kai Hu,[1] Jichun Lian,[1] Li Zhu,[2] Qinjun Chen,[1,*] and Sheng-Yi Xie[1,†]
[1]*School of Physics and Electronics, Hunan University, Changsha, 410082, China*
[2]*Geophysical Laboratory, Carnegie Institution for Science, Washington, DC 20015, USA*

(Received 13 December 2019; revised manuscript received 12 March 2020; accepted 25 March 2020; published 17 April 2020)

Fe_2P-type dioxides are significant both for geoscience and condensed-matter physics. For example, Fe_2P-type SiO_2 has been proposed to be one of the dominant components in the mantles of super-Earths and Fe_2P-type TiO_2 has been shown to have a large visible absorbance. Here we report the discovery of an Fe_2P-type phase in a typical transition-metal dichalcogenide (TMD), $TiTe_2$, using crystal structure prediction and first-principles calculations. Ambient layered $TiTe_2$ will first transform to a monoclinic $C2/m$ phase and then finally to the hexagonal Fe_2P-type phase above 33 GPa. Fe_2P-type $TiTe_2$ is predicted to be metallic, contrasting with the semiconductivity of Fe_2P-type TiO_2. The same high-pressure phase (Fe_2P type) appears both in transition-metal dioxides and TMDs, indicating that the stacking patterns of anions and cations play an increasingly important role in determining the high-pressure phase.

DOI: 10.1103/PhysRevB.101.134109

I. INTRODUCTION

Fe_2P is an important mineral on earth. In the past, it attracted the research interest of material scientists mainly due to the magnetic properties such as the magnetic anisotropy, to serve as a potential candidate for permanent magnet applications [1]. Recently, Fe_2P nanoparticles were proposed to own considerably high discharge capacities and excellent rate capability applied in nickel-based rechargeable batteries [2]. Additionally, many dioxides were proposed to transform to this phase under pressure. The high-pressure Fe_2P-type SiO_2 was proposed as one of the dominant components in the mantles of super-Earths [3], and Fe_2P-type TiO_2 was demonstrated to have a large visible absorbance, in contrast with that of ambient rutile TiO_2 [4]. Other Fe_2P-type dioxides, such as ZrO_2 [5], CrO_2 [6], and VO_2 [7], were also proposed under compression by experiment or theory.

With the anions identified as the same group-VI elements, transition-metal dichalcogenides (TMDs) have attracted extensive interest due to their exotic physical properties [8–11]. As a typical TMDs, $TiTe_2$ have a layered sandwich structure with weak van der Waals (vdW) interactions for the interlayers. It has a wide range of applications in electronics and optoelectronics [12], exhibiting extraordinary properties such as charge-density waves [13,14], superconductivity [15–17], and Fermi-liquid semimetallicity [18,19]. Previous studies have suggested that external pressure can modulate the electronic properties of TMDs. $TiTe_2$ undergoes band inversion under hydrostatic pressure, resulting in a topological phase transition [20,21]. Pressure can also change the crystal structures either through atomic rearrangement or symmetry breaking. In nature, the pressure of the vacuum in the universe is only 10^{-15} Pa (or lower), while the highest pressure inside some neutron stars can reach up to 10^{35} Pa [22]. In laboratory, a recent study reported a realized hydrostatic pressure above 750 GPa [23]. Thus, the pressure can serve as a powerful pool to produce new phases and tune the properties of a crystal. Recently, a study reported that the ambient trigonal $P\text{-}3m1$ $TiTe_2$ undergoes a phase transformation to a monoclinic $C2/m$ phase at 8 GPa, and the two phases will coexist up to 16 GPa, as has been experimentally confirmed by synchrotron x-ray diffraction (XRD) and Raman spectroscopy in a diamond-anvil cell [24]. Two other studies have also supported the phase transition to the monoclinic $C2/m$ phase with only some differences in the exact transformation pressure, using infrared phonon spectra [25] and electronic transport measurements [26], but further investigations of the structural evolution of $TiTe_2$ under strong compression have thus far been absent.

Here, we study the stable $TiTe_2$ phases up to 100 GPa using crystal structure prediction and first-principles calculations. Our calculations support the existence of the structural transition from the $P\text{-}3m1$ phase to $C2/m$ phase, which agrees with previous experimental results [24–26]. Further, we predict hexagonal Fe_2P-type $TiTe_2$ to be stable above 33 GPa, which is much smaller than that of SiO_2 (690 GPa) and for TiO_2 (161 GPa). The compression will activate the lone-pair p electrons of ambient layered $TiTe_2$ to form the covalent bond, thereby completing the phase transformation to $C2/m$ and finally to the Fe_2P-type phase. The present work suggests a typical route from ambient layered TMDs to high-pressure three-dimensional covalent bond linked structures under compression.

II. COMPUTATIONAL METHODS

The structural evolution of CALYPSO [27] is performed with the particle-swarm optimization (PSO) algorithm within

---

[*] chenqj@hnu.edu.cn
[†] shengyi_xie@hnu.edu.cn

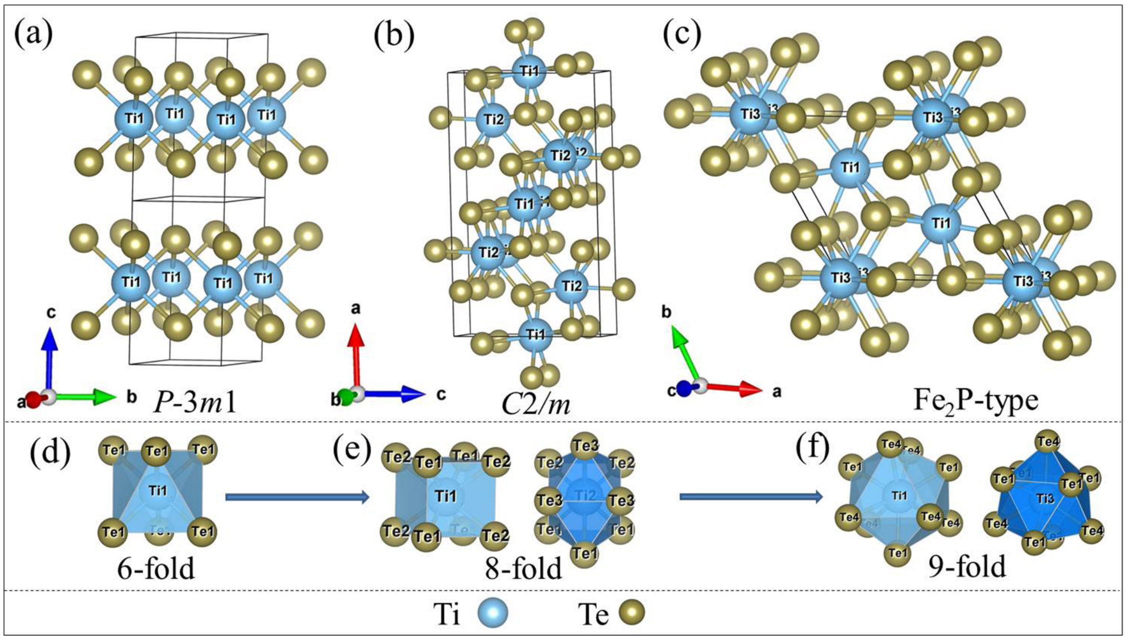

FIG. 1. Crystal structures for (a) the ambient trigonal (space group P-3m1, $Z = 1$) phase, (b) the high-pressure monoclinic (space group $C2/m$, $Z = 6$) phase, and (c) the high-pressure hexagonal Fe_2P-type structure (space group P-62m, $Z = 3$) of $TiTe_2$. The coordination polyhedra of the three phases are shown for (d) the P-3m1 phase, (e) the $C2/m$ phase (marked with Ti1 and Ti2 for 2d and 4i positions, respectively), and (f) the Fe_2P-type structure (marked with Ti1 and Ti3 for 2d and 1a positions, respectively). The cyan and golden-brown balls separately represent Ti and Te atoms.

the evolutionary scheme. Basically, CALYPSO explores the potential-energy surface to find the most stable (lowest in energy or free energy) structure of a large assembly of atoms. CALYPSO will first generate random structures (the number of individual structures defines the size of the population) symmetrically constrained within 230 space groups [28]. The 60% lowest-enthalpy structures of each generation were used to produce the structures in the next generation by PSO technique, and the remaining 40% structures were randomly generated within symmetry constraint to enhance the structural diversity. Typically, the structure searching simulation for each calculation was stopped after we generated 1000 ∼ 1200 structures (e.g., about 20∼30 generations). We chose the $TiTe_2$ simulation cells ranging from 2 to 6 formula units at 0, 25, 50, 75, and 100 GPa and the structure search was performed with a population size of 30 structures per generation and up to 50 generations in our searching, which usually will guarantee the convergence of searching with the system smaller than 20 atoms. The structural relaxations and total-energy calculations were based on density-functional theory, and were inserted into the Vienna *Ab initio* Simulation Package [29]. The generalized gradient approximation (GGA) with the Perdew-Burke-Ernzerhof (PBE) functional [30] and the projector augmented wave (PAW) method [31] were used in all the calculations. Additionally, other pseudopotential and functional such as the ultrasoft pseudopotential (USPP) [32], local density approximation (LDA) [33], and Perdew-Wang 91 (PW91) [34], were used to compare the transition pressures with that of PBE. To accurately describe the electronic properties, the hybrid functional (HSE06) was applied [35]. The phonon dispersions were calculated with the supercell approach [36], which was implemented in the PHONOPY code [37] The energy cutoff for the plane-wave basis was set to 500 eV and a k-point resolution was chosen with $2\pi \times 0.03$ Å^{-1}. The maximum force of the atoms was

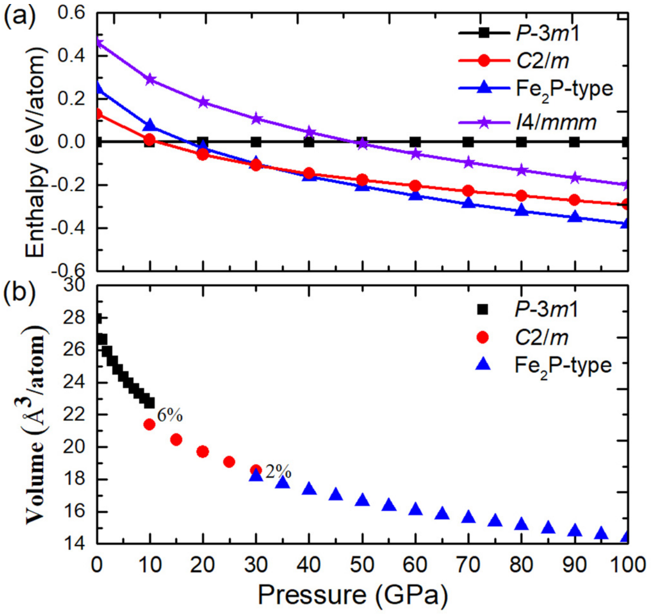

FIG. 2. Enthalpy and volume curves as a function of pressure for $TiTe_2$ from 0 to 100 GPa. (a) The relative enthalpy up to 100 GPa with the ambient P-3m1 phase as a reference. (b) The volume variation with pressure for the P-3m1, $C2/m$, and Fe_2P-type phases. At the transition pressures of 12 and 33 GPa, the $C2/m$ phase and the Fe_2P-type phase show 6 and 2% volume decrements, respectively.

TABLE I. Structural information for $TiTe_2$ phases, including the space group, cell parameters, and Wyckoff positions.

Pressure	Space group	Lattice parameters (Å)	Wyckoff position
0 GPa	P-3m1	$a = b = 3.778$; $c = 6.72$ $\alpha = \beta = 90^\circ$; $\gamma = 120^\circ$	Ti:1b (0, 0, 1/2) Te:2d (1/3, 2/3, 0.244)
20 GPa	$C2/m$	$a = 13.556$; $b = 3.380$; $c = 7.746$ $\alpha = \gamma = 90^\circ$; $\beta = 91.761^\circ$	Ti:2d (0, 1/2, 1/2) Ti:4i (0.184, 1/2, 0.753) Te:4i (0.156, 0, 0.474) Te:4i (0.972, 0, 0.192) Te:4i (0.325, 0, 0.889)
33 GPa	Transition state (P-1)	$a = 3.445$; $b = 6.728$; $c = 7.653$ $\alpha = 102.277^\circ$; $\beta = 84.337^\circ$; $\gamma = 75.496^\circ$	Ti:2i (−0.417, 0.199, −0.221) Ti:1h (−1/2, −1/2, −1/2) Te:2i (−0.156, −0.187, −0.501) Te:2i (−0.240, 0.093, 0.164) Te:2i (−0.127, −0.470, −0.167)
50 GPa	Fe_2P-type	$a = b = 7.320$; $c = 3.232$ $\alpha = \beta = 90^\circ$; $\gamma = 120^\circ$	Ti:2d (1/3, 2/3, 1/2) Ti:1a (0, 0, 0) Te:3g (0.275, 0.725, 1/2) Te:3f (0.388, 0.388, 0)

less than 0.01 eV/Å for each ionic relaxation. The transition state and related energy barrier were calculated by a pathway sampling method via swarm intelligence and graph theory [38]. The synchrotron x-ray-diffraction patterns of $TiTe_2$ were simulated within the MERCURY 4.2 software package [39].

III. RESULTS AND DISCUSSION

As shown in Fig. 1(a), the ambient 1T-$TiTe_2$ crystal has a layered hexagonal CdI_2-type structure (space group P-3m1, No. 164) [40,41]. In this phase, titanium (Ti) forms six bonds with surrounding tellurium (Te) atoms to build an octahedron [Fig. 1(d)]. Under pressure, the P-3m1 phase will transform to a monoclinic $C2/m$ phase [Fig. 1(b), space group No. 12] with an eightfold coordination of Ti [Fig. 1(e)], which was confirmed by many experimental groups. A study of Raman spectroscopy and synchrotron x-ray-diffraction experiment suggested that the phase transition takes place at 8 GPa, yet the two phases coexist until the P-3m1 phase vanishes at 16 GPa [24]. The high-pressure electrical transport measurement study proposed that the transition occurs at 5.4 GPa and the P-3m1 phase disappears completely at 19.1 GPa [26]. Infrared spectroscopic measurements study suggested the transition at 12 GPa [25]. Notably, the coexistence of original and transformed phases under cold compression was reported in other oxides [42], which may be related with the complex dynamic growth of the phase. For TMDs, the phase transition from P-3m1 to $C2/m$ under pressure appears to be general and occurs in TaS_2 at 20 GPa [43] and $IrTe_2$ at 5 GPa [41]. By further compression, our crystal structure searching predicts that the $C2/m$ phase will transform into a hexagonal ninefold-coordinated Fe_2P-type structure [space group P-62m, No. 189, Figs. 1(c) and 1(f)] at 33 GPa, as indicated from the enthalpy-pressure curves in Fig. 2(a). The detailed lattice parameters and Wyckoff positions for these three $TiTe_2$ phases are listed in Table I. The transition pressures determined by other potentials and functionals such as USPP, PAW-LDA, and PAW-PW91 were approximate with that of PAW-PBE, as shown in Table II. Thus, the description of Fe_2P-type crystal structure within PBE is applicable. Additionally, the vdW interaction has some influence on the first phase transition from P-3m1 to $C2/m$ phase (with the transition pressure of 12/14 GPa with/without vdW corrections), but has little effect on the transition pressure from $C2/m$ to Fe_2P-type phase (both are 33 GPa). This may originate from that the vdW interaction plays a role in determining the layered ambient P-3m1 phase rather than the compressed $C2/m$ and Fe_2P-type phases.

Interestingly, the Fe_2P-type phase was already discovered in dioxides as an important high-pressure phase. For example, previous studies suggested that Fe_2P-type SiO_2 may be one of dominant components in the mantles of super-Earths [3] and Fe_2P-type TiO_2 has a large visible absorbance [4] in contrast with that of ambient rutile or anatase TiO_2. However, the required pressures for Fe_2P-type dioxides are much higher than those for $TiTe_2$ (690, 161, and 100 GPa for SiO_2 [3], TiO_2 [4], and VO_2 [7], respectively), due to the much smaller atomic radius and the larger electronegativity of oxygen. As shown in Fig. 2(b), the volume of $TiTe_2$ drops by approximately 6% and 2% to facilitate the transformation to the $C2/m$ and

TABLE II. Transition pressures for $C2/m$ and Fe_2P-type structures with different pseudopotential and functional.

Phase	Transition pressure	Method
$C2/m$	12 GPa	PBE
	14 GPa	PBE+D
	13 GPa	PW91
	8 GPa	LDA
	8 GPa	USPP
Fe_2P-type	33 GPa	PBE
	33 GPa	PBE+D
	33 GPa	PW91
	32 GPa	LDA
	30 GPa	USPP

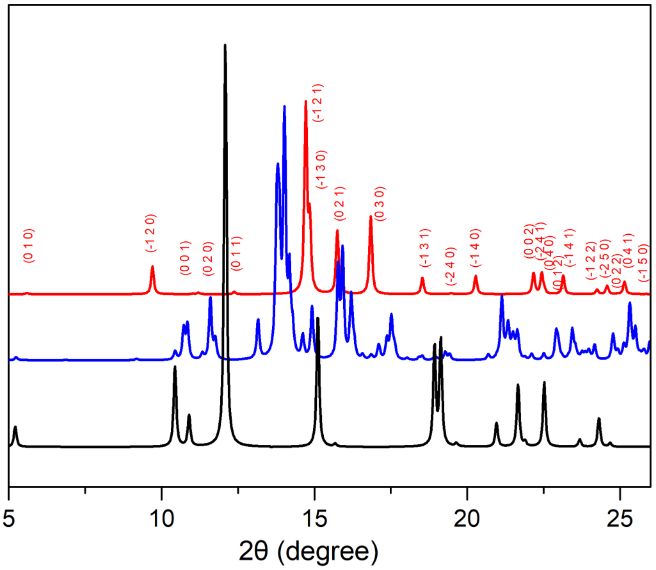

FIG. 3. Simulated synchrotron XRD patterns ($\lambda = 0.6199$ Å) of the P-3m1 phase at 0 GPa (black line), the $C2/m$ phase at 20 GPa (blue line), and the Fe_2P-type structure at 50 GPa (red line). The Miller indices ($h\ k\ l$) for the diffraction peaks of the Fe_2P-type $TiTe_2$ are marked.

Fe_2P-type phases at the corresponding transition pressures of 12 and 33 GPa, respectively. The densification of $TiTe_2$ under compression is realized by increasing the cation coordination number from 6 in P-3m1 phase to 8 in $C2/m$ phase and finally to 9 in Fe_2P-type phase. The space-group symmetries also evolve along with the variation of the coordination polyhedrons of the three phases. The ambient P-3m1 $TiTe_2$ owns a high-symmetry hexagonal lattice with six Te atoms equivalent around the centered Ti to form an octahedron, as illustrated in Fig. 1(d). When it transforms to $C2/m$ phase under pressure, the equivalent octahedron in P-3m1 phase evolves into two different coordination polyhedra in Fig. 1(e). Accordingly, the hexagonal symmetry of the lattice is broken and degenerates to monoclinic. With further transformation to Fe_2P phase, however, the symmetry of crystal lattice restores to be hexagonal.

X-ray diffraction is a typical technique used to determine crystal structures and a previous experiment provided the Rietveld refinement of the synchrotron XRD pattern of the P-3m1 phase at 0.36 GPa [24]. Another high-pressure experiment suggested that the XRD patterns of the $C2/m$ phase have a prominent peak appearing at around 10.5° with increasing pressure up to 20 GPa [26]. The simulated synchrotron XRD pattern of Fe_2P-type $TiTe_2$ alongside the ambient P-3m1 and high-pressure $C2/m$ phases are plotted in Fig. 3 with $\lambda = 0.6199$ Å, in order to be consistent with that of previous experiment [26]. The Miller indices ($h\ k\ l$) for the XRD peaks of the Fe_2P-type $TiTe_2$ are marked as a reference for future experiments. Compared with the $C2/m$ phase, the XRD peaks of Fe_2P-type $TiTe_2$ decrease dramatically due to the improvement in the crystal symmetry, and the main XRD peak of the Fe_2P-type phase derived from the (-1 2 1) plane shifts to a higher diffraction angle with 2θ at 14°. The variation of XRD peaks of the three phases is directly related with the change of crystal symmetry. The high-symmetry P-3m1 and Fe_2P phases, which also have more equivalent atoms in a unit cell, have fewer diffraction peaks compared with the low-symmetry $C2/m$ phase.

To verify the dynamic stability of the three phases of $TiTe_2$, we calculated the phonon dispersion curves as illustrated in Fig. 4. The calculated results suggest that all three $TiTe_2$ phases are dynamically stable. Under compression, the vibrational frequencies of the optical branches for the high-pressure $C2/m$ and Fe_2P-type phases significantly increase compared to the ambient P-3m1 phase, indicating that the pressure strengthens the interaction between cations and anions.

At the transition pressure of 33 GPa, $C2/m$ phase still has no dynamical instability or soft phonons mode. Thus, there is an energy barrier between the $C2/m$ and Fe_2P-type phase to prevent the spontaneous phase transformation. As shown in Fig. 5(a), the energy barrier estimated by our calculation is 0.29 eV/atom, which is far beyond the room-temperature thermal kinetic energy. Thus, high temperature or exceeding

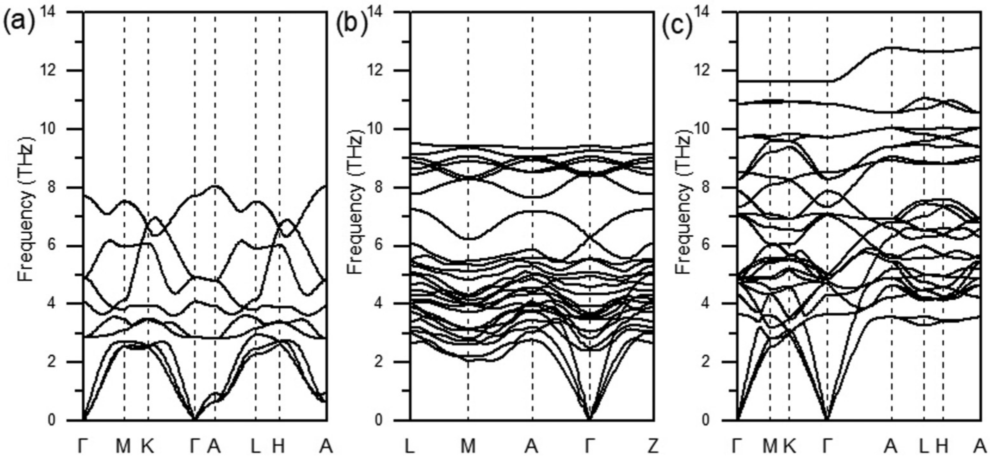

FIG. 4. Calculated phonon band structures of (a) the P-3m1 phase at 0 GPa, (b) the $C2/m$ phase at 20 GPa, and (c) the Fe_2P-type structure at 50 GPa.

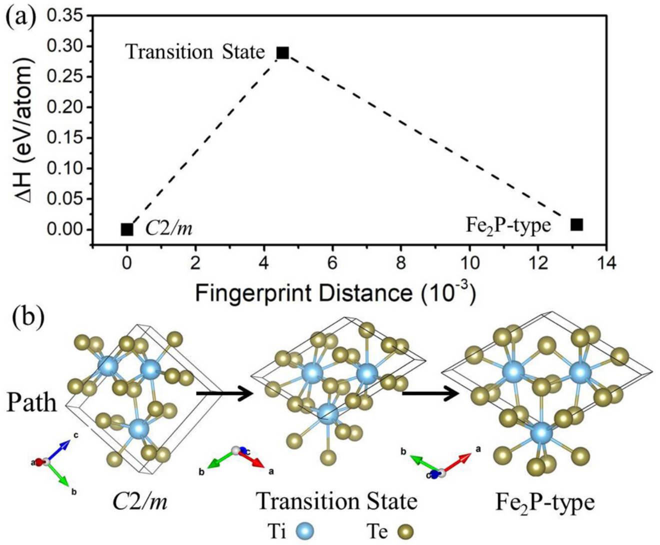

FIG. 5. (a) Energy barrier between the initial $C2/m$ and final Fe_2P-type structure at 33 GPa. The $C2/m$ phase was chosen as a reference for enthalpy. (b) Phase transition pathway for $C2/m$ to Fe_2P-type structure. To illustrate clearly, here we gave the primitive cell of $C2/m$ phase.

the transition pressure estimated from total-energy calculation may be necessary to achieve the phase transformation observed in experiment, just as the transformation from wurtzite to diamond structure of silicon occurs at high temperature above 600 °C [44]. The crystal structure of the transition state was illustrated in Fig. 5(b) and the lattice information is listed in Table I.

As illustrated in Fig. 6, we calculated the relevant electronic properties including the PBE and HSE06 band structure and the corresponding electronic densities of states (DOS) of the $TiTe_2$ phases. Generally, the dispersion of electronic band between PBE and HSE06 is similar, yet the exact eigenvalues of the band have some differences. The ambient $P\text{-}3m1$ $TiTe_2$ phase is metallic with two large electronic pockets at points M and L, as shown in Fig. 6(a). At the Fermi level, the flat band along Γ-A indicates the weak van der Waals interaction of interlayers and the large bandwidth along the Γ-M-K-Γ path originates from the strong interaction of the sandwichlike intralayer of $TiTe_2$. As shown in Figs. 6(b) and 6(c), both the $C2/m$ and Fe_2P-type phases are also metallic due to the partial overlap of the Te p and Ti d bands. Interestingly, the previously reported Fe_2P-type structures of TiO_2 have a band gap of 0.66 eV at 160 GPa, and the gap does not vanish until the Fe_2P-type structure transforms to the $I4/mmm$ phase at a pressure of up to 647 GPa [45]. From the DOS diagram in Fig. 6(d), it is seen that the d electrons of Ti mainly contribute to states around the Fermi level and the p electrons of Te mainly contributed to states −2 to −1 eV below the Fermi level, which is consistent with the previous reports [46]. As shown in Figs. 6(e) and 6(f), the d electrons of Ti in the $C2/m$ phase and the Fe_2P-type structure gradually become dominant at low energies of −2 to −1 eV with increasing pressure. It can also be observed that both the $C2/m$ phase and

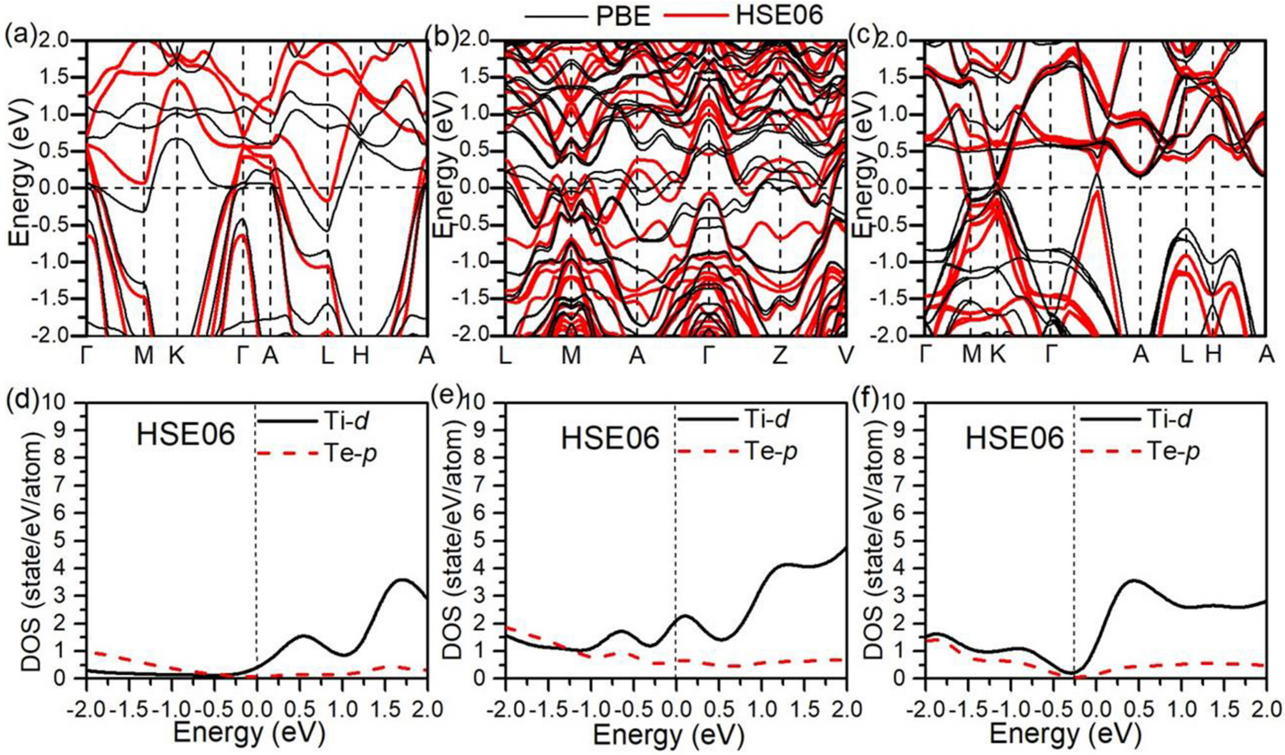

FIG. 6. Electronic properties of $TiTe_2$ using PBE (black line) and hybrid functional HSE06 (red line) within the spin-orbit coupling effect: electronic band structure for (a) $P\text{-}3m1$ phase at 0 GPa, (b) $C2/m$ phase at 20 GPa, and (c) Fe_2P-type structure at 50 GPa. (d)–(f) Corresponding DOS of HSE06.

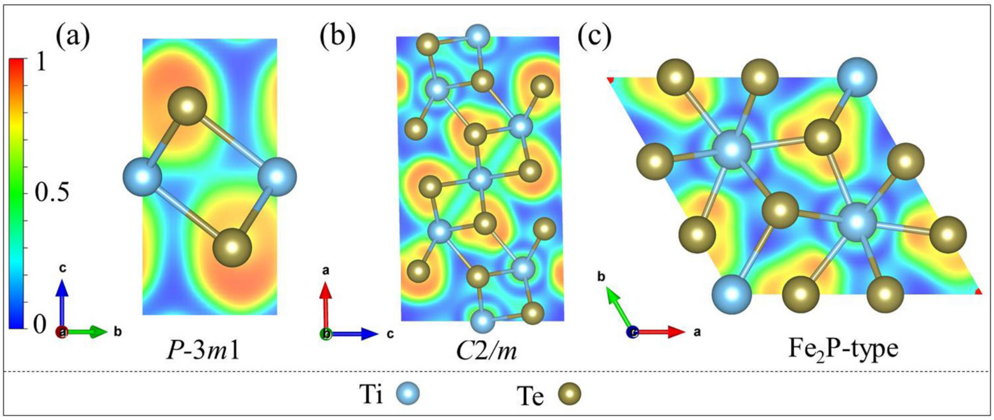

FIG. 7. The 2D ELF $TiTe_2$ for (a) P-3m1 phase in (1 0 0) plane, (b) $C2/m$ phase in (0 1 0) plane, and (c) Fe_2P-type structure in (0 0 1) plane.

Fe_2P-type structure have a consistent electronic distribution at high pressure.

To further understand the atomic bonding, the projected two-dimensional (2D) electron localization functions (ELFs) of the $TiTe_2$ phases are shown in Fig. 7. ELF is used to characterize the localized distribution of electrons. The ELF was originally proposed by Becke and Edgecombe to measure electron pairing by defining $\mathrm{ELF} = (1 + \chi_\sigma^2)^{-1}$, where $\chi_\sigma = D_\sigma / D_\sigma^0$ (σ-spin electron), and $D_\sigma = \tau_\sigma - \frac{1}{4}\frac{(\nabla\rho_\sigma)^2}{\rho_\sigma}$, $D_\sigma^0 = \frac{3}{5}(6\pi^2)^{2/3}\rho_\sigma^{5/3}$, where D_σ^0 corresponds to a uniform electron gas with spin density equal to the local value of $\rho_\sigma(\boldsymbol{r})$, τ_σ is the positive-definite kinetic-energy density defined by $\tau_\sigma = \sum_i^\sigma |\nabla\psi_i|^2$, and the ratio χ_σ is thus a dimensionless localization index calibrated with respect to the uniform-density electron gas as reference [47]. They used uniform electron gas as a reference system, and normalized the function so that its value was between 0 and 1 [47]. The ELF values of 1, 0.5, and close to 0 indicate strong electron, electron gas, and nonelectron localizations, respectively. The ELF of the layered P-3m1 phase approaching 1 was far away from the Te–Ti bond, which is typical for the lone-pair electrons. For the compressed $C2/m$ phase, some lone-pair electrons of Te still remain, yet some of them are transferred to the region of the Ti–Te bond. For the Fe_2P-type phase, the high-ELF region completely moves to the Ti–Te bond region to form a covalent bond. Hence, the compression will compel the lone-pair p electrons of Te in the layered P-3m1 phase to participate in the chemical bonding under compression, realizing the high-pressure $C2/m$ phase and Fe_2P-type structure with an increase in the coordination number.

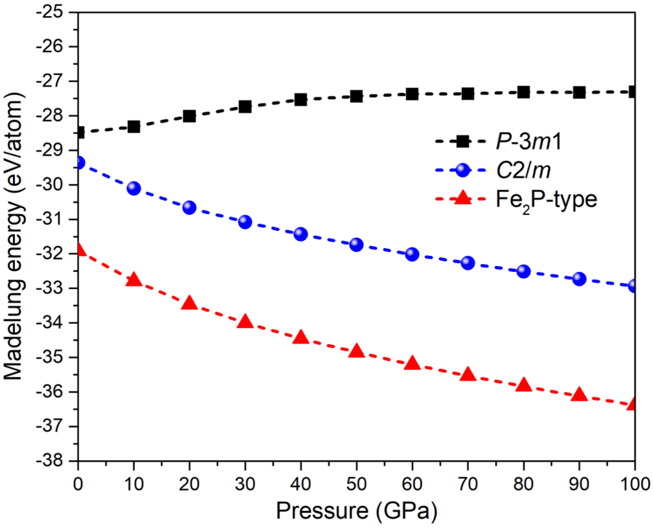

FIG. 8. The Madelung energy with pressure for the P-3m1, $C2/m$, and Fe_2P-type phases.

It is very interesting to compare the ambient-pressure and high-pressure phases of transition-metal dioxides and TMDs (e.g., TiO_2 [4,45] and $TiTe_2$). Usually, ambient transition-metal dioxides prefer a three-dimensional covalent bond structure, such as the rutile and anatase TiO_2 [48]. Instead, the ambient TMDs favor layered structures due to the distinguishing physical or chemical properties of chalcogen, such as its large atomic radius and small electronegativity compared to that of oxygen. However, the same high-pressure phase appears in TMDs (Fe_2P-type $TiTe_2$ and $I4/mmm$ TaS_2 [43]) with transition-metal dioxides suggesting that the difference in anions becomes noncrucial. Instead, the special packing of anions and cations plays an increasingly significant role in determining the stable compressed phase for the TMDs. The Madelung energy in Fig. 8, defined as the energy of Coulomb interaction between crystal lattice with a simple assumption of $-2e$ for Te and $+4e$ for Ti, clearly shows the stacking patterns of anions and cations have a relatively weak influence at ambient pressure but with an increasingly strong effect on determining the above three $TiTe_2$ phases under pressure. Notably, due to the limited calculation resources, the unit cell of our structure searing is constrained within a maximum of 6 formula, thus the possibility of more complex crystal lattices beyond Fe_2P-type phase is excluded in the present study and it deserves further theoretical and experimental explorations.

IV. CONCLUSIONS

Using crystal structure predictions and first-principles calculations, we predicted a ninefold-coordinated Fe_2P-type phase of $TiTe_2$ under pressure. Our calculations suggest that the layered P-3m1 $TiTe_2$ will first transform to an eightfold-coordinated $C2/m$ phase, which agrees with previous experiment studies [24–26], and then to the Fe_2P-type $TiTe_2$ phase above 33 GPa. The transition pressure of Fe_2P-type $TiTe_2$ is much smaller than that phase of dioxides due to the large atomic radius and small electronegativity of Te. Our ELF analysis shows that the lone-pair p electrons of Te will be activated to form a covalent bond with Ti under compression to realize the phase transformation. The totally different ambient structures but existence of the same high-pressure phase (Fe_2P type) for transition-metal dioxides and TMDs indicates that the stacking patterns of anions and cations to realize special coordination play an increasingly important role in determining the high-pressure phases.

ACKNOWLEDGMENTS

We would like to acknowledge the financial support of the National Natural Science Foundation of China (Grants No. 11704111 and No. 11604093) and the Fundamental Research Funds of the Central Universities (Grant No. 531107050916). We also are grateful for the TianHe-1 supercomputer in Changsha and the Artificial Microstructure Science and Technology Collaborative Innovation Center Cluster at Nanjing University for providing calculation resources.

[1] H. Fujii, T. Hokabe, T. Kamigaichi, and T. Okamoto, J. Phys. Soc. Jpn. **43**, 41 (1977).
[2] Y. P. Wang, L. L. Zhang, H. H. Li, Y. J. Wang, L. F. Jiao, H. T. Yuan, L. Chen, H. Tang, and X. F. Yang, J. Power Sources **253**, 360 (2014).
[3] T. Tsuchiya and J. Tsuchiya, Proc. Natl. Acad. Sci. USA **108**, 1252 (2011).
[4] H. Dekura, T. Tsuchiya, Y. Kuwayama, and J. Tsuchiya, Phys. Rev. Lett. **107**, 045701 (2011).
[5] D. Nishio-Hamane, H. Dekura, Y. Seto, and T. Yagi, Phys. Chem. Miner. **42**, 385 (2014).
[6] S. X. Huang, X. Wu, J. J. Niu, and S. Qin, RSC Adv. **8**, 24561 (2018).
[7] S. Y. Xie, L. H. Wang, F. Y. Liu, X. B. Li, L. G. Bai, V. B. Prakapenka, Z. H. Cai, H. K. Mao, S. B. Zhang, and H. Z. Liu, J. Phys. Chem. Lett. **9**, 2388 (2018).
[8] J. A. Wilson and A. D. Yoffe, Adv. Phys. **18**, 193 (1969).
[9] R. A. Klemm, Physica C **514**, 86 (2015).
[10] Q. H. Wang, K. Kalantar-Zadeh, A. Kis, J. N. Coleman, and M. S. Strano, Nat. Nanotechnol. **7**, 699 (2012).
[11] J. A. Wilson, D. Salvo, and S. Mahajan, Adv. Phys. **50**, 1171 (2001).
[12] K. S. Novoselov, A. Mishchenko, A. Carvalho, and A. H. Castro Neto, Science **353**, aac9439 (2016).
[13] P. Chen, Y. H. Chan, X. Y. Fang, Y. Zhang, M. Y. Chou, S. K. Mo, Z. Hussain, A. V. Fedorov, and T. C. Chiang, Nat. Commun. **6**, 8943 (2015).
[14] M. M. May, C. Brabetz, C. Janowitz, and R. Manzke, Phys. Rev. Lett. **107**, 176405 (2011).
[15] B. Sipos, A. F. Kusmartseva, A. Akrap, H. Berger, L. Forro, and E. Tutis, Nat. Mat. **7**, 960 (2008).
[16] U. Dutta, P. S. Malavi, S. Sahoo, B. Joseph, and S. Karmakar, Phys. Rev. B **97**, 060503(R) (2018).
[17] P. B. Allen and N. Chetty, Phys. Rev. B **50**, 14855 (1994).
[18] R. Claessen, R. O. Anderson, J. W. Allen, C. G. Olson, C. Janowitz, W. P. Ellis, S. Harm, M. Kalning, R. Manzke, and M. Skibowski, Phys. Rev. Lett. **69**, 808 (1992).
[19] R. Claessen, R. O. Anderson, and G. H. Gweon, Phys. Rev. B **54**, 2453 (1996).
[20] M. Zhang, X. Wang, A. Rahman, Q. Zeng, D. Huang, R. Dai, Z. Wang, and Z. Zhang, Appl. Phys. Lett. **112**, 041907 (2018).
[21] Q. Y. Zhang, Y. C. Cheng, and U. Schwingenschlögl, Phys. Rev. B **88**, 155317 (2013).
[22] R. R. Silbar and S. Reddy, Am. J. Phys. **72**, 892 (2004).
[23] L. Dubrovinsky, N. Dubrovinskaia, E. Bykova, M. Bykov, V. Prakapenka, C. Prescher, K. Glazyrin, H.-P. Liermann, M. Hanfland, M. Ekholm, Q. Feng, L. V. Pourovskii, M. I. Katsnelson, J. M. Wills, and I. A. Abrikosov, Nature (London) **525**, 226 (2015).
[24] V. Rajaji, U. Dutta, P. C. Sreeparvathy, S. C. Sarma, Y. A. Sorb, B. Joseph, S. Sahoo, S. C. Peter, V. Kanchana, and C. Narayana, Phys. Rev. B **97**, 085107 (2018).
[25] U. Dutta, S. Sahoo, P. S. Malavi, F. Piccirilli, P. Di Pietro, A. Perucchi, S. Lupi, and S. Karmakar, Phys. Rev. B **99**, 125105 (2019).
[26] Y. H. Zhou, C. H. Chen, Y. Zhou, X. L. Chen, C. C. Gu, C. An, B. W. Zhang, Y. F. Yuan, H. Wu, R. R. Zhang, L. L. Zhang, X. D. Zhu, X. P. Yang, and Z. R. Yang, Phys. Rev. B **99**, 125104 (2019).
[27] Y. C. Wang, J. Lv, L. Zhu, and Y. M. Ma, Comput. Phys. Commun. **183**, 2063 (2012).
[28] Y. C. Wang, J. Lv, L. Zhu, and Y. M. Ma, Phys. Rev. B **82**, 094116 (2010).
[29] G. Kresse and J. Furthmüller, Phys. Rev. B **54**, 11169 (1996).
[30] J. P. Perdew, K. Burke, and M. Ernzerhof, Phys. Rev. Lett. **77**, 3865 (1996).
[31] P. E. Blochl, Phys. Rev. B: Condens. Matter **50**, 17953 (1994).
[32] D. Vanderbilt, Phys. Rev. B **41**, 7892 (1990).
[33] J. P. Perdew and A. Zunger, Phys. Rev. B **23**, 5048 (1981).
[34] J. P. Perdew and Y. Wang, Phys. Rev. B **45**, 13244 (1992).
[35] A. V. Krukau, O. A. Vydrov, A. F. Izmaylov, and G. E. Scuseria, J. Chem. Phys. **125**, 224106 (2006).
[36] K. Parlinski, Z. Q. Li, and Y. Kawazoe, Phys. Rev. Lett. **78**, 4063 (1997).
[37] A. Togo, F. Oba, and I. Tanaka, Phys. Rev. B **78**, 134106 (2008).
[38] L. Zhu, R. E. Cohen, and T. A. Strobel, J. Phys. Chem. Lett. **10**, 5019 (2019).
[39] C. F. Macrae, P. R. Edgington, P. McCabe, E. Pidcock, G. P. Shields, R. Taylor, M. Towler, and J. van de Streek, J. Appl. Crystallogr. **39**, 453 (2006).
[40] Y. Arnaud and M. Chevreton, J. Solid State Chem. **39**, 230 (1981).
[41] J. M. Léger, A. S. Pereira, J. Haines, S. Jobic, and R. Brec, J. Phys. Chem. Solids **61**, 27 (2000).

[42] R. L. Tang, Y. Li, S. Y. Xie, N. N. Li, J. H. Chen, C. X. Gao, P. W. Zhu, and X. Wang, Sci. Rep. **6**, 38566 (2016).

[43] K. Hu, Q. J. Chen, and S. Y. Xie, J. Phys.: Condens. Matter **32**, 085402 (2019).

[44] R. J. Kobliskat and S. A. Sojin, Phys. Rev. B **8**, 3799 (1973).

[45] M. J. Lyle, C. J. Pickard, and R. J. Needs, Proc. Natl. Acad. Sci. USA **112**, 6898 (2015).

[46] D. K. G. de Boer, C. F. van Bruggen, G. W. Bus, R. Coehoorn, C. Haas, G. A. Sawatzky, H. W. Myron, D. Norman, and H. Padmore, Phys. Rev. B **29**, 6797 (1984).

[47] A. D. Becke and K. E. Edgecombe, J. Chem. Phys. **92**, 5397 (1990).

[48] Z. Fu, Y. C. Liang, S. M. Wang, and Z. Zhong, Phys. Status Solidi B **250**, 2206 (2013).